Philosophical Magazine,
Vol. 86, No. 16, 1 June 2006, 2329–2342

Taylor & Francis
Taylor & Francis Group

Translation and orientation domain boundaries in $La_{2/3}Ca_{1/3}MnO_3$

YONG DING†‡ and Z. L. WANG*‡

†Institut für Festkörperforschung, Forschungszentrum
Jülich GmbH, D-52425 Jülich, Germany
‡School of Materials Science and Engineering, Georgia Institute
of Technology, Atlanta, GA 30332-0245, USA

(*Received 6 September 2005; in final form 21 November 2005*)

From crystal structure, three types of translation and two types of orientation domain boundaries are expected in $La_{2/3}Ca_{1/3}MnO_3$ as a result of phase transition. However, the most easily observed domain boundaries in the bulk samples are $[\frac{1}{2}\frac{1}{2}\frac{1}{2}]$ translation boundaries (or antiphase boundaries) and 90° domain boundaries, while the $[\frac{1}{2}0\frac{1}{2}]$ and $[0\frac{1}{2}0]$ translation boundaries were rarely observed. In this paper, this phenomenon is explained by considering the tilting modes of the oxygen octahedra in the structure. We found that there is no distortion to the nearby oxygen octahedra if the $[\frac{1}{2}\frac{1}{2}\frac{1}{2}]$ translation boundaries take the (010) boundary planes and the 90° domain boundaries are in the {101} planes, making them low-energy boundary planes and, thus, are easy to form. On the other hand, the $[\frac{1}{2}0\frac{1}{2}]$ and $[0\frac{1}{2}0]$ translation boundaries introduce a distortion in the oxygen octahedra, which requires breaking the tilting modes in the boundary areas and, therefore, they are high-energy boundary planes, which are rarely observed. The above-expected results are supported by our transmission electron microscopy data.

1. Introduction

Perovskite compounds have attracted a significant research interest due to their fascinating electrical and magnetic properties [1, 2]. Most of these properties are directly related to the displace phase transition from the basic perovskite structure to a more complicated perovskite-derived structure. Domain and domain boundaries appear after the phase transition, a consequence of the lower symmetry [3, 4]. Geometrically, the formation of the domains and domain boundaries can be related to the distortion of the basic ABO_3 perovskite unit [5–9]. Three types of distortions have been identified [5]: distortion of the oxygen octahedra, B-type cation displacement within the octahedra and the tilting of the octahedra relative to one another as practically rigid corner-linked units. These three types of distortions have successfully been used in characterization of the structure of the low symmetry phases.

*Corresponding author. Email: zhong.wang@mse.gatech.edu

Philosophical Magazine
ISSN 1478–6435 print/ISSN 1478–6443 online © 2006 Taylor & Francis
http://www.tandf.co.uk/journals
DOI: 10.1080/14786430500519780

In this work, we report the investigation of domains and domain boundaries in perovskite-derived oxides based on the tilting of oxygen octahedra. $La_{2/3}Ca_{1/3}MnO_3$, a material that has colossal magnetoresistance (CMR), is selected as the sample in the present study, since both orientation and translation domain boundaries are present in this material [10–15]. The effect of domain rotation and magneto-crystalline anisotropy distribution in determining the anisotropic transport properties of the $La_{2/3}Ca_{1/3}MnO_3$ thin films with different growth orientations is discussed [16]. Knowledge on the domain structures will benefit our understanding of the strain effect on properties [17]. Moreover, it was suggested that the translation boundaries or antiphase boundaries (APBs) might be related to the La and Ca distribution [12]. In the following, we first analyze the domain boundary structures in $La_{2/3}Ca_{1/3}MnO_3$, based on the oxygen octahedron tilting modes, then, we show the experimental results of transmission electron microscopy (TEM). In the final section, the formation of these domains, domain boundaries and their relations are discussed.

2. Oxygen octahedron tilting modes of the domain boundaries in $La_{2/3}Ca_{1/3}MnO_3$

Based on the assumption that oxygen octahedra are arranged regularly throughout the bulk, Glazer [6, 7] suggested a convenient way to describe oxygen octahedra tilting in terms of sub-tilting around the axes of the pseudo-cubic perovskite unit cell. Each of the octahedron connects directly with six other octahedra along $\pm x$, $\pm y$ and $\pm z$ directions. Considering the rigid connection at the corner of the oxygen octahedra and without shifting the center of the octahedra away from the axes, it becomes apparent that a clockwise tilting of an octahedron around one of the three axes, for example, the z-axis, determines the anti-clockwise tilting mode along the same z-axis, of the four octahedra connected with this one along $\pm x$ and $\pm y$ directions. Meanwhile, the two octahedra along the tilting axis, z-axis, are flexible and need to be specified with a tilting, in either the same or opposite mode, depending on the crystal structure. This is illustrated in figure 1. These shifted oxygen atoms of the centre octahedron will draw four oxygen octahedra connected from $\pm x$ and $\pm y$ directions, respectively, to tilt anti-clockwise around the z-tilting axis (figure 1a), while the two octahedra connected from $\pm z$ directions can tilt either clockwise (figure 1b) or anti-clockwise (figure 1c) along the z-tilting axis. Therefore, only the tilting modes along the tilting axis, needed to specify the tilting modes in the plane perpendicular to the tilting axis, are uniquely defined. There are three totally independent tilting axes: we define the tilt modes for a system using symbols $\boldsymbol{\alpha}^{\#}\boldsymbol{\beta}^{\#}\boldsymbol{\gamma}^{\#}$. The sequence of the letters refers to the tilting axes as $a_p \sim [100]_p$, $b_p \sim [010]_p$ and $c_p \sim [001]_p$ axis of the pseudo-cubic perovskite unit, respectively. The letters of $\boldsymbol{\alpha}$, $\boldsymbol{\beta}$ and $\boldsymbol{\gamma}$ stand for the tilting level (angles). The superscript # specifies the tilting of the connected oxygen octahedra along the tilting axis, the values can be ***zero***, ***s*** or ***o***, indicating no tilting, tilting in the same or in the opposite mode, respectively. In the case of figure 1b and c, the tilting mode along $c_p \sim z$ axis can be described as ***s*** and ***o***, respectively. There are 23 possible basic tilting systems and the space group of these systems can be directly derived from the tilting modes [7].

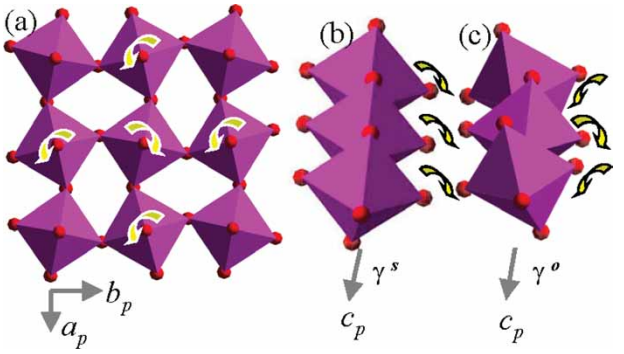

Figure 1. Schematic diagram showing octahedra tilting modes. The tilting axis is $c_p \sim [001]_P$. In (a), the centre octahedron tilts around c_p clockwise, the octahedra connected with $\pm a_p$ and $\pm b_p$ directions tilt anticlockwise along the c_p axis. The octahedra connected with the $\pm c_p$ axis can tilt either clockwise (b) or anticlockwise, corresponding to the indexed tilting modes, as γ^s and γ^o, respectively. Here, γ gives the tilting angle around $c_p \sim [001]_P$ axis.

The room temperature phase of $La_{2/3}Ca_{1/3}MnO_3$ has an orthorhombic structure with the space group *Pnma* and lattice parameters $a \approx c \approx \sqrt{2}a_p$, $b = 2a_p$, where a_p is the lattice parameter of the pseudo-cubic perovskite unit cell [18, 19]. In the notation of the oxygen octahedron tilting model, the structure can be described as $\boldsymbol{\alpha^o\beta^s\gamma^o}$. Figures 2a and b show the schematic diagram of the configuration of the octahedra in two adjacent layers stacking along the z-axis (defined to be the normal of the paper plane). Omitting the tilting level around each axes, we can specify the tilting states of every oxygen octahedra in the crystal if the tilting configuration of one oxygen octahedron is defined. In figure 2a, we arbitrarily choose the tilting state of octahedron at the top-left position 000 in the first layer as positive '+++' about the basic $[100]_p$, $[010]_p$ and $[001]_p$ axes, which are the [101], [010] and $[10\bar{1}]$ axes of the $La_{2/3}Ca_{1/3}MnO_3$ *Pnma* phase, respectively. The detailed tilting states of other oxygen octahedra in reference to the (0,0,0) octahedron can be deduced from the rule of $\boldsymbol{\alpha^o\beta^s\gamma^o}$ and are shown in figures 2a and b. Taking an example, consider the oxygen octahedron located at $(\frac{1}{2}, 0, \frac{1}{2})$ as shown in figures 2a and d, because this octahedron is connected with 000 octahedron along $[100]_p$, only the tilting state around $[100]_p$ direction is decided by the rule of $\boldsymbol{\alpha^o\beta^s\gamma^o}$. The other two tilting states along $[010]_p$ and $[001]_p$ should take the opposite state of 000 octahedron taken. $\boldsymbol{\alpha^o}$ means opposite tilting mode between the connected octahedra along the tilting axis, the (0,0,0) octahedron takes positive +, then the $(\frac{1}{2}, 0, \frac{1}{2})$ octahedron take −. Therefore, the tilting state of the $(\frac{1}{2}, 0, \frac{1}{2})$ octahedron should be −−−. In the same way, the tilting modes of the octahedra at the positions of $(\frac{1}{2}, \frac{1}{2}, \frac{1}{2})$ and $(0\,\frac{1}{2}\,0)$ are '+−+' and '−+−', respectively. Figures 1c and d are the same, but indexed using different unit cells, which give the relationship between the basic perovskite unit cell and larger real unit cell, for example, $[010]_p = \frac{1}{2}[010]$, $[100]_p = \frac{1}{2}[101]$.

Both orientation and translation domain boundaries were expected in $La_{2/3}Ca_{1/3}MnO_3$ based on the space group analysis [10]. The orientation boundaries include 90° and 120° boundaries. Three types of translation boundaries or antiphase

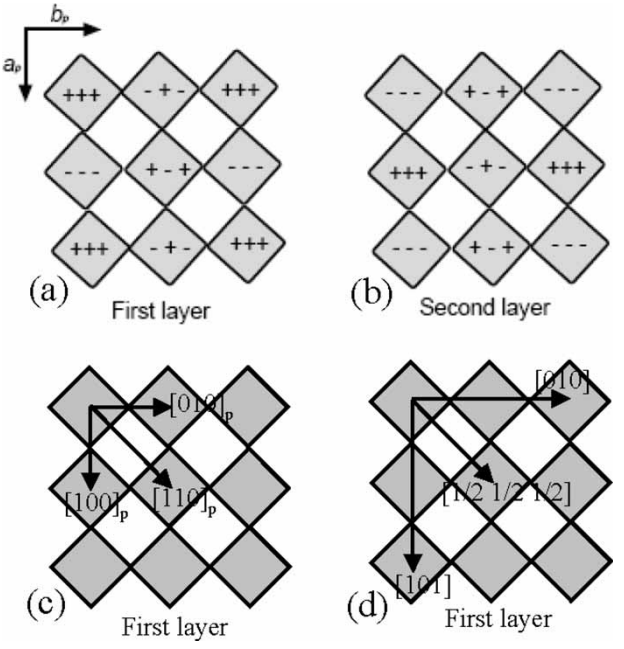

Figure 2. Schematic diagram of the tilting modes for (a) the first and (b) second layers of octahedra in $La_{2/3}Ca_{1/3}MnO_3$ described by $\boldsymbol{\alpha^o\beta^s\gamma^o}$. The diagram in (c) and (d) are the same but indexed using the basic perovskite unit cell and larger real unit cell, respectively.

boundaries (APBs) are characterized by the $[\frac{1}{2}\frac{1}{2}\frac{1}{2}]$, $[\frac{1}{2}0\frac{1}{2}]$ and $[0\frac{1}{2}0]$ translations, respectively.

Based on this structural feature, two translation domains or antiphase domains $\boldsymbol{T}$ and $\boldsymbol{T}'$ can be related through the $(010)_p$ boundary plane from one to the other by the $[\frac{1}{2}\frac{1}{2}\frac{1}{2}]$ translation without violating the corner-sharing configuration of the neighbouring oxygen octahedra. As shown in figure 3, the octahedron with the '+++' tilting mode in domain $\boldsymbol{T}$ changes to the '+−+' tilting mode in domain $\boldsymbol{T}'$ due to the boundary translation. Checking the tilting configuration of the octahedra beside the boundary plane, the tilting modes of the oxygen octahedra in domain $\boldsymbol{T}$ are '−+−' and '+−+', against the tilting modes of '+−+' and '−+−' in domain $\boldsymbol{T}'$. Both of them show the opposite tilts around the a_p, b_p and c_p directions. In comparison to the tilting modes in the perfect area, just the tilting around the b_p axis shows a different sense, the opposite sense. On the other hand, since the two adjacent octahedra across the (010) boundary plane have a common b_p axis, the tilting mode around the axis is flexible, i.e. they can be either opposite or same sense. These different senses neither violate the rule of the tilting modes nor induce distortion in the oxygen octahedra. Only a slight distortion in the interstitial spaces surrounded by eight oxygen octahedra is induced in comparison with those inside of each domain. Thus, the (010) APBs should be low-energy boundaries.

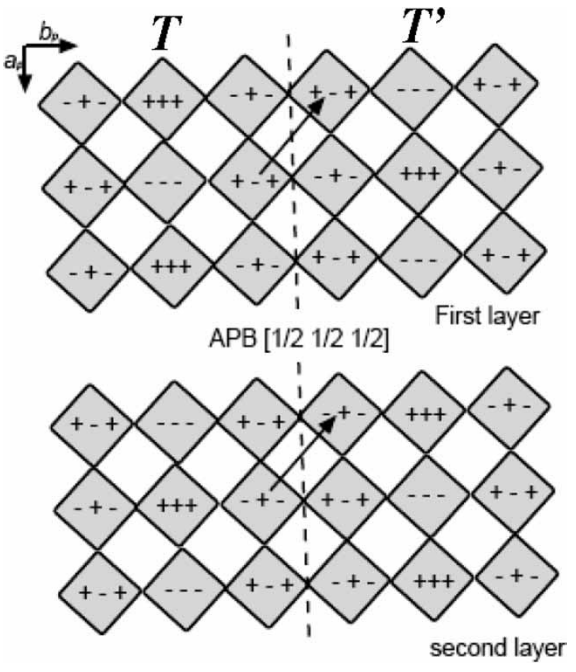

Figure 3. Schematic diagrams of the oxygen octahedra tilting modes along a $[\frac{1}{2}\frac{1}{2}\frac{1}{2}]$ translation APB. The boundary plane is $(010)_p$ plane denoted by dashed lines. No oxygen octahedra are distorted along the boundary.

Substituting the '$---$' or '$-+-$' for the '$+-+$' tilting mode in $\boldsymbol{T}'$, two other antiphase boundaries are formed, which are characterized by $[\frac{1}{2}0\frac{1}{2}]$ and $[0\frac{1}{2}0]$ displacements, respectively. In these two cases, distortion of the oxygen octahedra is unavoidable due to the direct violation of the tilting mode configuration in the octahedra beside the boundary plane. The system energy is expected to be seriously increased due to the distortion.

For the two orientation domains $\boldsymbol{O_{90}}$ and $\boldsymbol{O'_{90}}$ related by a 90° tilting around the b_p axis, the a_p and c_p axes are exchanged across the boundary plane [10]. Thus, the $a_p\ b_p\ c_p$ of the domain $\boldsymbol{O_{90}}$ change to $-c_p\ b_p\ a_p$ of the domain $\mathbf{O'_{90}}$. In this system the oxygen octahedra tilting classification $\boldsymbol{\alpha^o\beta^s\gamma^o}$ still remains unchanged. We take the (101) plane as the boundary, as shown in figure 4. The difference between the two domains is in the change of the tilting modes in an opposite way along the a_p axis of domain $\boldsymbol{O'_{90}}$ due to the change of c_p to $-a_p$ across the domain boundary. For example, in the domain $\boldsymbol{O'_{90}}$ the first octahedron directly below the boundary has a mode '$-++$' instead of '$+++$'. This shows the same situation for the oxygen octahedra beside the boundary plane as the APB discussed above. In this case, the slight distortion of the spaces surrounded by the eight oxygen octahedra beside the 90° domain boundary is introduced by the change of the tilting modes for the a_p axis from opposite to the same orientation across the boundary. Therefore, the 90° boundary with its boundary perpendicular to the a_p axis, i.e. the

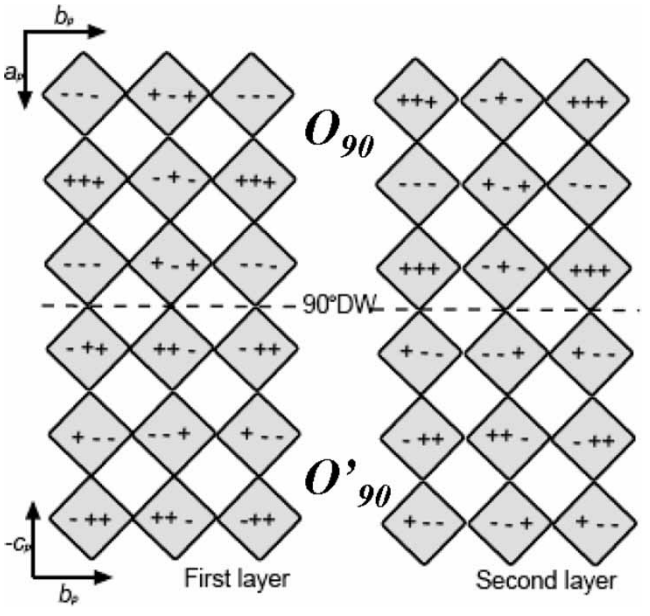

Figure 4. Schematic diagrams of the oxygen octahedra tilting modes along a 90° domain boundary. The boundary is in (101) plane and marked by dashed lines. No oxygen octahedra are distorted along the boundary.

{101} planes in the *Pnma* phase, the same, is expected to be a low-energy boundary. It is expected that the formation energy of the $[\frac{1}{2}\frac{1}{2}\frac{1}{2}]$ translation APB and the 90° orientation domain boundaries is comparable. A small energy difference can be due to the different tilting angles around the a_p and b_p axes.

In the case of 120° domain boundaries, the domains beside the boundary are related by a 120° rotation around a $\langle 111\rangle_p$ axis. The tilting classification changes from domain $\boldsymbol{O_{120}}$ to $\boldsymbol{O'_{120}}$ can be described as $\boldsymbol{\alpha^o\beta^s\gamma^o}$ to $\boldsymbol{\beta^s\alpha^o\gamma^o}$. We did not find the 120° domain boundary with no distortion of the oxygen octahedra. If the $(110)_p$ plane, the (121) planes in *Pnma* phase, is chosen as the boundary plane, a relatively low density of distorted oxygen octahedra can be obtained, as shown in figure 5. The distorted oxygen octahedra are marked by '**?**'. The formation energy of such a type of boundary is expected to be higher than that of the $[\frac{1}{2}\frac{1}{2}\frac{1}{2}]$ translation boundary and the 90° orientation boundary, but lower than those of the $[\frac{1}{2}0\frac{1}{2}]$ and $[0\frac{1}{2}0]$ translation boundaries.

As discussed by Sapriel [20], the orientation domain boundaries are formed to maintain strain compatibility between adjacent domains. The point symmetry operators lost during phase transition not only crystallographically relates one orientation domain to another, but also the strain tensor of one domain to the tensor of another. Therefore, the planes in which the strain tensor is kept unchanged are the possibly low-energy boundaries. In the case of $La_{2/3}Ca_{1/3}MnO_3$ *Pnma* phase, such planes of the 90° and 120° domain boundaries are the {101} and the {121} planes, respectively. This agrees with the above results deduced from oxygen octahedra tilting modes, as discussed.

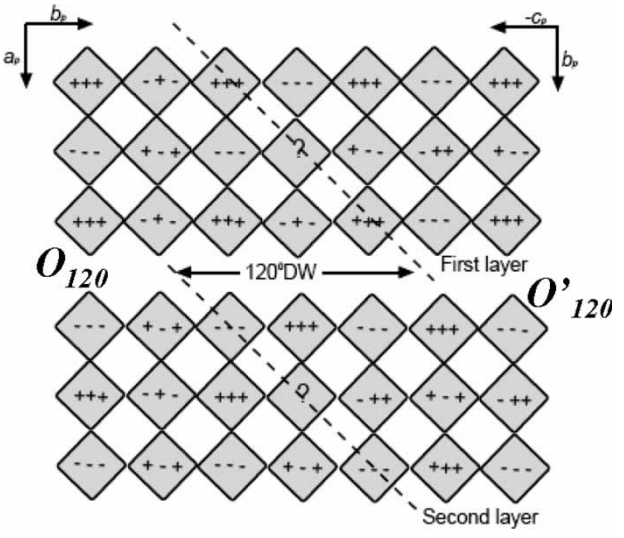

Figure 5. Schematic diagram of the oxygen octahedra titling modes along a 120° domain boundary. The distorted octahedra are marked by '**?**'.

3. Experimental results

The samples for TEM investigations are ceramic $La_{2/3}Ca_{1/3}MnO_3$, synthesized using the solid-state reaction method. Compared to the samples used in our previous study [12, 13], the samples used in this paper were annealed at 1000°C for 72 h to fully relax the domain boundaries and get the stable boundary planes. TEM specimens were prepared by a standard procedure of mechanical polishing, dimpling and ion-milling. A Philips CM20 electron microscope was used to record diffraction patterns and diffraction contrast images. The high-resolution transmission electron microscopic (HRTEM) observation was carried out using a JEM 4000EX microscope operated at 400 kV.

Figure 6 shows three dark-field images formed by the diffractions of (111), (010) and (213) spots. Associated with the formation of 120° domains, the rotation around $\langle 111\rangle_p$ by 120° changes the axes a_p, b_p and c_p to b_p, c_p and a_p, or c_p, a_p and b_p, depending on the rotation direction. As a consequence, the (111) diffraction of domain $\boldsymbol{O'_{120}}$ will overlap, with respect to domain $\boldsymbol{O_{120}}$, with the reciprocal-space lattice point of $(\frac{1}{2}2\bar{\frac{1}{2}})$ (not a real diffraction spot here) or $(\frac{3}{2}0\bar{\frac{1}{2}})$ (not a real diffraction spot here); the (010) diffraction overlaps with the reciprocal-space lattice point of $(\frac{1}{2}0\bar{\frac{1}{2}})$ (not a real diffraction spot here) or $(\frac{1}{2}0\frac{1}{2})$ (not a real diffraction spot here); and (213) diffraction overlaps with the reciprocal-space lattice point of $(05\bar{1})$ (a real diffraction spot) or $(3\bar{1}\bar{2})$ (not a real diffraction spot here). Thus, the domains having 120° rotation relationship will show opposite contrast in the dark-field images formed by the diffraction spots (111) and (010). For, the domain showing bright contrast due to the contribution of (111) and (010) diffractions across the 120° domain boundaries, the other domain will be dark due to no real diffraction from this domain passing through the objective aperture. As discussed in section 2,

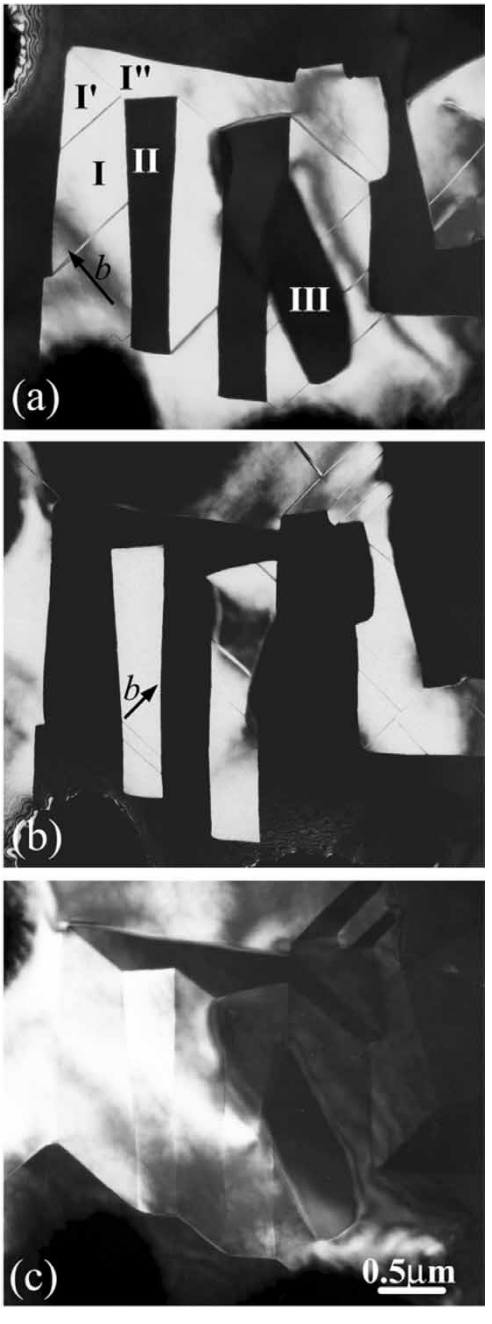

Figure 6. Dark-field images formed using the diffraction spots of (a) (111), (b) (010), and (c) (213). The boundaries between domains I and II, I′ and I″, and I and I' are 120° domain boundary, 90° domain boundary, and $[\frac{1}{2}\frac{1}{2}\frac{1}{2}]$ translation APB, respectively.

across a 90° domain boundary, the domains share a common b_p axis, whilst the a_p and c_p axes of domain $\boldsymbol{O'_{90}}$ change to c_p and $-a_p$, respectively. Rotating by 90° around the b_p axis, the diffraction spot (111) will overlap with reciprocal-space spot of $(11\bar{1})$ (also a real diffraction spot) and the diffraction spot (213) will overlap with $(31\bar{2})$ (not a real diffraction spot here). Thus, the 90° orientation domains show the same contrast in the dark-field images formed by the diffraction spots (111) and (010), but opposite contrast in the dark-field image formed by the (213) diffraction spot. Keeping above rules in mind and checking the contrast behavior of the domains shown in figure 6a–c, we know that the boundaries between I and II, and I″ and II, were determined to be 120° domain boundaries, and that between I′ and I″ is a 90° domain boundary.

Figures 7a–c show three selected-area electron diffraction (SAED) patterns taken from the I, II, and III areas shown in figure 6a. All of the bright areas in figure 6a have the same diffraction pattern as shown in figure 7a, with the electron beam parallel to $[100]_p$ or [101] direction. The electron beams of the patterns in figures 7b and c are parallel $[\bar{1}01]$ (or $[001]_p$) and [010] (or $[010]_p$) directions, respectively. The patterns in figures 7b and c can be reproduced by rotating the pattern in figure 7a by $\pm 120°$ around the axis of $[111]_p$, which means that domain I and domain II form a 120° domain boundary.

The orientations of the domain boundaries in figure 6 can be determined from the rotation angle between the SAED patterns and their edge-on conditioned boundary images. The $\boldsymbol{b}$ (same as b_p) axis of some domains is marked by the arrows in figure 6. It shows that the 90° domain boundary between domains I′ and I″ is a $(100)_p$, i.e. the (101) plane and the 120° domain boundaries between I and II, and I″ and II, are in the $(110)_p$, i.e. the (121) planes.

In figure 6a, we can also find a different type boundary between domains I and I′. They show no contrast in the image of figure 6c formed by the (213) reflection. According to the criterion under two beam conditions, the APBs show contrast if $2\pi \cdot \boldsymbol{g} \cdot \mathbf{R} = (2n+1)\pi$ ($\boldsymbol{g}$ is the diffraction corresponded reciprocal vector, $\boldsymbol{R}$ is the characterized translation between the two contacted domains; n is an integer). Considered the contrast behavior of the boundaries in figure 6 and combined with the SAED patterns in figure 7, the boundary between domain I and domain I′ can be classified as an APB associated with $[\frac{1}{2}\frac{1}{2}\frac{1}{2}]$ translation. This type of APB was found to have a high density and always lie in the (010) plane.

Only a few grains contain the APBs associated with the $[\frac{1}{2}0\frac{1}{2}]$ and $[0\frac{1}{2}0]$ translations. Figures 8a and b show two dark-field images formed by the $(1\bar{1}1)$ and (211) diffractions, respectively. Based on the above criteria for APB contrast, the lines in figure 8a can be related to the APB with either $[\frac{1}{2}\frac{1}{2}\frac{1}{2}]$ or $[0\frac{1}{2}0]$ translation. In figure 8b, the line boundary showing contrast corresponds to the APB associated with $[\frac{1}{2}0\frac{1}{2}]$ or $[0\frac{1}{2}0]$ translation. Therefore, considered the two images together, the boundaries between I and II, and I′ and II′, that show contrast in both figures 8a and b should be the APB associated with $[0\frac{1}{2}0]$ translation. The boundaries between I and I′, II and II′, and II′ and II″, which appear only in figure 8a, are the APBs taking the translation vector of $[\frac{1}{2}\frac{1}{2}\frac{1}{2}]$. The boundaries between I and II′ and I′ and II″, showing contrast only in figure 8b, are the $[\frac{1}{2}0\frac{1}{2}]$ translation-related APBs.

Figure 9 is a HRTEM image of an APB with the $[\frac{1}{2}\frac{1}{2}\frac{1}{2}]$ translation shown in figure 6. The incident electron beam is parallel to $[10\bar{1}]$ (or $[100]_p$) direction.

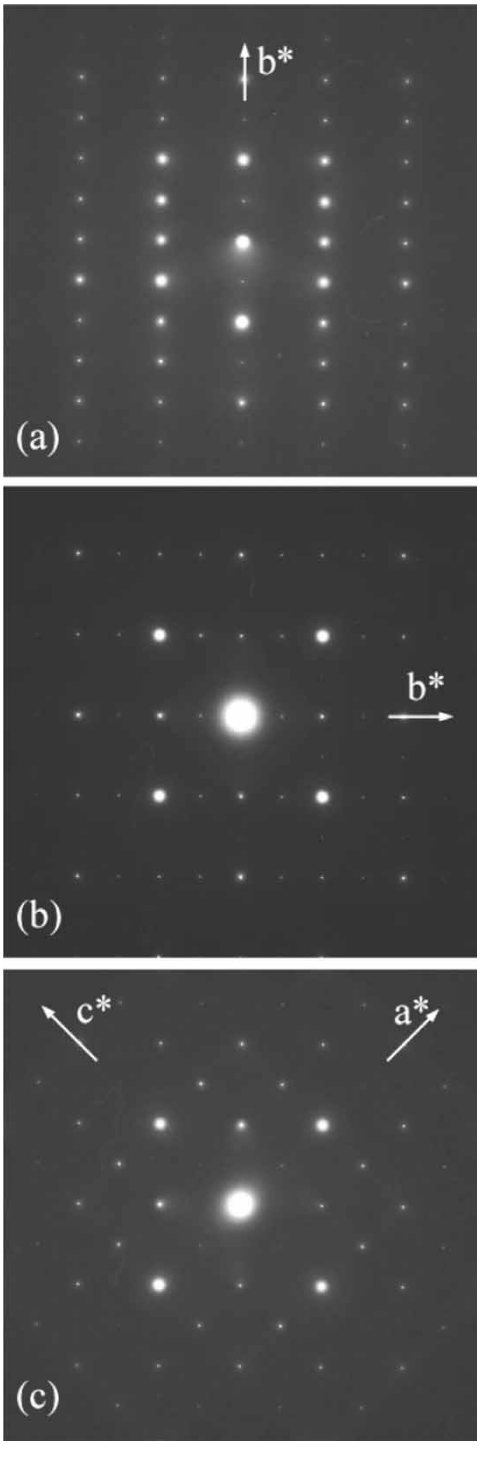

Figure 7. SAED patterns of the domains (a) I, (b) II, and (c) III shown in figure 6a.

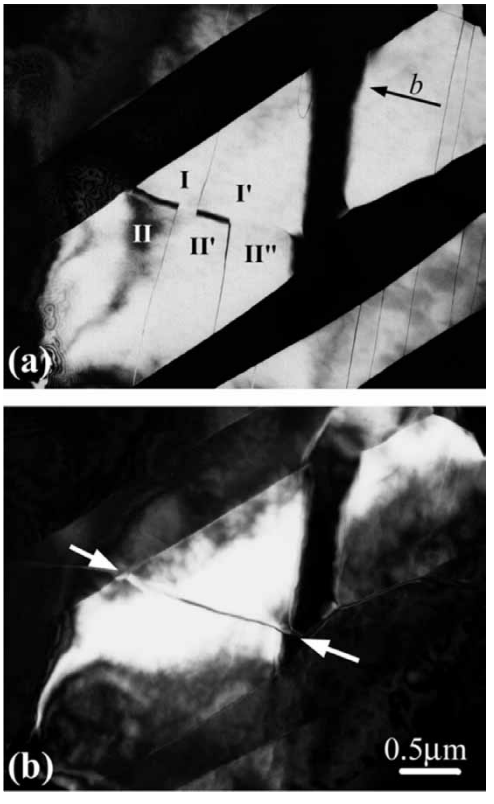

Figure 8. Two dark-field images using the diffraction spots (a) (111) and (b) (211). The boundaries between domains I and II, I and II′, and I and I′ are the APBs with $[0\,\frac{1}{2}0]$, $[\frac{1}{2}0\,\frac{1}{2}]$ and $[\frac{1}{2}\frac{1}{2}\frac{1}{2}]$ translations, respectively.

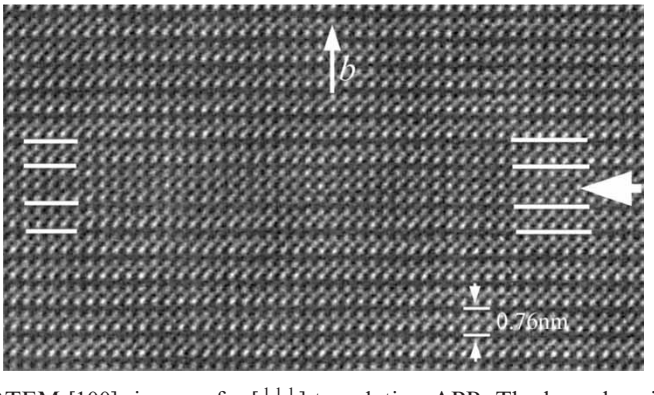

Figure 9. HRTEM $[100]_p$ image of a $[\frac{1}{2}\frac{1}{2}\frac{1}{2}]$ translation APB. The boundary is in the $(010)_p$ plane and marked by an arrow head.

The doubled translation symmetry along b axis is due to the different tilting states of the octahedra. Thus, the appearance of the triplicate lines corresponds to an APB instead of a stacking fault. Across the APB denoted by an arrow head, the top and the bottom domains are related by a $[0\frac{1}{2}0]$ translation, which is the projected component of the translation $[\frac{1}{2}\frac{1}{2}\frac{1}{2}]$ along the [101] direction. The domain boundary is clearly lying in the (010) plane.

4. Discussion

The configuration of the domains and domain boundaries observed by TEM and HRTEM shows good agreement with our analysis based on the oxygen octahedra tilting modes. The APBs with $[\frac{1}{2}\frac{1}{2}\frac{1}{2}]$ translation are perpendicular to $\boldsymbol{b}$ axis, resulting in a low energy configuration: continuity of corner-sharing oxygen octahedra and the smallest distortion of the interstitial space across the boundary plane. For the same reason, the 90° domain boundaries prefer to lying in the {101} (or $\{100\}_p$) plane. Since the APBs with $[\frac{1}{2}0\frac{1}{2}]$ and $[0\frac{1}{2}0]$ translations break down the above low energy configuration, they are seldom observed in TEM experiments.

The formation of APBs is well understood in the *order–disorder* phase transition in multiple component systems [21, 22]. Above the transition temperature, different atoms randomly occupy the atom positions. After cooling down below the transition temperature, different types of atomic occupancy at different positions changes the symmetry of the system, leading to the formation of domains and the antiphase boundaries. APB is one type of the most common domain boundaries. In these systems, the movement of an APB requires the diffusion of the atoms in the boundary-swept areas. In contrast, for the perovskite oxide materials, the difference between high and low temperature phases is, in many cases, just a tiny local shift of atoms. The shift of the domain boundaries then occurs comparably easily, for they do not need to move atoms from one position to another as in the case of the domains formed in *order–disorder* transitions. So, when an APB forms in the perovskite-derived structured materials, it always tends to adjust itself to lie in its low energy boundary plane, just like the APBs associated with $[\frac{1}{2}\frac{1}{2}\frac{1}{2}]$ translation; (010) is such a boundary plane.

It is well accepted that the size of the A-site cation influences the tilting distortion of the octahedron framework [23]. Moreover, the conventional ceramic sintering technique applied for the complex oxide preparation often suffers from inhomogeneity in the cation distribution, resulting in a variation of composition for different grains within the bulk sample. On the other hand, the distortion of the oxygen octahedral, induced by the inhomogeneous distribution of the A site cations, can sometimes compensate for the distortion caused by the lattice deformation in the boundary areas. In this way, the boundaries can be stabilized [12]. Therefore, in the as-sintered materials, we can often find the $[\frac{1}{2}0\frac{1}{2}]$ and $[0\frac{1}{2}0]$ translation boundaries and the $[\frac{1}{2}\frac{1}{2}\frac{1}{2}]$ translation APBs with the boundary planes other than the low-energy (010) plane. After a long time annealing, the distribution of A site cations La and Ca, becomes uniform. The $[\frac{1}{2}\frac{1}{2}\frac{1}{2}]$ translation APBs taking the high energy boundaries and the $[\frac{1}{2}0\frac{1}{2}]$ and $[0\frac{1}{2}0]$ translation boundaries become less stable

and their density is largely reduced. The most common APBs are lying in (010) plane and characterized by $[\frac{1}{2}\frac{1}{2}\frac{1}{2}]$ translation. This is the configuration of the domain boundaries observed in the annealed sample.

A phase transition is always accompanied by spontaneous strain. If a grain is constrained by the surroundings, the orientation domains are formed to keep the grain in its original shape [20, 24, 25]. The strain compatibility between two adjacent domains determines the boundary plane. These orientation domains in $La_{2/3}Ca_{1/3}MnO_3$ are 90° and 120° domains. The lattice distortion of the 90° domain boundaries is smaller than that of the 120° domain boundaries. However, according to our analysis, the formation of the 120° domains is effective in maintaining the grain shape.

5. Conclusion

Domains and domain boundaries in $La_{2/3}Ca_{1/3}MnO_3$ were investigated by TEM and HRTEM, and discussed in terms of tilting modes of the oxygen octahedra. The $[\frac{1}{2}\frac{1}{2}\frac{1}{2}]$ translation boundaries or antiphase boundaries in (010) planes and 90° domain boundaries in {101} planes were found to preserve the corner-sharing and distortion-free oxygen octahedra along the boundaries. These boundaries appear very sharp and straight in experimental images. Part of the oxygen octahedra were distorted at the (121) 120° orientation boundaries, whereas all of the oxygen octahedra beside the $[\frac{1}{2}0\frac{1}{2}]$ and $[0\frac{1}{2}0]$ APBs suffered distortion. Inhomogeneous distribution of the A site cations is expected to stabilize the $[\frac{1}{2}0\frac{1}{2}]$ and $[0\frac{1}{2}0]$ APBs and the $[\frac{1}{2}\frac{1}{2}\frac{1}{2}]$ APBs with boundary planes other than the (010) low-energy planes. Annealing treatment homogenized the distribution of the A site cations and, thus, reduced the density of the relatively high energy boundaries.

Acknowledgements

The authors would like to thank Dr Q. Y. Xu for preparation of polycrystalline $La_{2/3}Ca_{1/3}MnO_3$ samples and Dr C. L. Jia, Dr S. B. Mi and Professor Dr K. Urban for fruitful discussion and modification of the manuscript. This work is supported by Forschungszentrum Jülich.

References

[1] J. F. Scott and C. A. Paz de Araujo, Science **246** 1400 (1989).
[2] S. Jin, T. H. Tiefel, M. McCormack, *et al*., Science **264** 413 (1994).
[3] M. Guymont, Phys. Rev. B **18** 5385 (1978).
[4] G. Van Tendeloo and S. Amelinckx, Acta Crystallogr. A **30** 431 (1974).
[5] C. J. Howard and H. T. Stokes, Acta Crystallogr. B **54** 782 (1998).

[6] A. M. Glazer, Acta Crystallogr. B **28** 3384 (1972).
[7] A. M. Glazer, Acta Crystallogr. A **31** 756 (1975).
[8] N. W. Thomas, Acta Crystallogr. B **52** 16 (1996).
[9] P. M. Woodward, Acta Crystallogr. B **53** 32 (1997); P. M. Woodward, Acta Crystallogr. B **53** 44 (1997).
[10] R. Wang, J. Gui, Y. Zhu, *et al*., Phys. Rev. B **63** 144106 (2001).
[11] M. Hervieu, G. Van Tendeloo, V. Caignaert, *et al*., Phys. Rev. B **53** 14274 (1996).
[12] Y. Ding and D. D. Liang, J. Appl. Phys. **92** 5425 (2002).
[13] D. D. Liang, C. H. Lei, Q. Y. Xu, *et al*., Phil. Mag. **83** 2915 (2003).
[14] M. Arita, A. Sasaki, K. Hamada, *et al*., J. Magn. Magn. Mater. **84** 84 (2000).
[15] Q. Chen, J. Tao, J. M. Zuo, *et al*., J. Mater. Res. **16** 2959 (2001).
[16] V. S. Amaral, C. S. Lourenço, J. P. Araujo, *et al*., J. Magn. Magn. Mater. **211** 1 (2002).
[17] R. B. Praus, G. M. Gross, F. S. Razavi, *et al*., J. Magn. Magn. Mater. **211** 41 (2002).
[18] O. Richard, W. Schuddinck, G. Van Tendeloo, *et al*., Acta Crystallogr. A **55** 704 (1999).
[19] P. G. Radaelli, D. E. Cox, M. Marezio, *et al*., Phys. Rev. B **55** 3015 (1997).
[20] J. Sapriel, Phys. Rev. B **12** 5128 (1975).
[21] M. Porta, C. Frontera, E. Vives, *et al*., Phys. Rev. B **56** 5261 (1997).
[22] J. Zhu and J. M. Cowley, Acta Crystallogr. A **38** 718 (1982).
[23] M. V. Lobanov, A. M. Balagurov, V. Ju. Pomjakushin, *et al*., Phys. Rev. B **61** 8941 (2000).
[24] J. Fousek and V. Janovec, J. Appl. Phys. **40** 135 (1969).
[25] K. Aizu, J. Phys. Soc. Jpn **28** 706 (1970).